

Simulation study of magnetic resonance imaging-guided cortically constrained diffuse optical tomography of human brain function

David A. Boas and Anders M. Dale

Diffuse optical imaging can measure brain activity noninvasively in humans through the scalp and skull by measuring the light intensity modulation arising from localized-activity-induced absorption changes within the cortex. Spatial resolution and localization accuracy are currently limited by measurement geometry to approximately 3 cm in the plane parallel to the scalp. Depth resolution is a more significant challenge owing to the limited angle tomography permitted by reflectance-only measurements. We combine previously established concepts for improving image quality and demonstrate, through simulation studies, their application for improving the image quality of adult human brain function. We show in a three-dimensional human head model that localization accuracy is significantly improved by the addition of measurements that provide overlapping samples of brain tissue. However, the reconstructed absorption contrast is significantly underestimated because its depth is underestimated. We show that the absorption contrast amplitude accuracy can be significantly improved by providing a cortical spatial constraint in the image reconstruction to obtain a better depth localization. The cortical constraint makes physiological sense since the brain-activity-induced absorption changes are occurring in the cortex and not in the scalp, skull, and cerebral spinal fluid. This spatial constraint is provided by segmentation of coregistered structural magnetic resonance imaging (MRI). However, the absorption contrast deep within the cortex is reconstructed superficially, resulting in an underestimation of the absorption contrast. The synthesis of techniques described here indicates that multimodality imaging of brain function with diffuse optical imaging and MRI has the potential to provide more quantitative estimates of the total and deoxyhemoglobin response to brain activation, which is currently not provided by either method independently. However, issues of depth resolution within the cortex remain to be resolved. © 2005 Optical Society of America

OCIS codes: 170.3010, 170.5280, 170.6960.

1. Introduction

The application of diffuse optical imaging (DOI) to the measurement of human brain function has been growing rapidly within the cognitive, behavioral, and neuroscience fields^{1–9}, following the early demonstrations that diffuse near-infrared light could be used to measure the hemodynamic response (i.e., blood flow, volume, and oxygenation) to brain activation in adult^{10,11} and infant^{12–14} humans, as well as the re-

cent commercial availability of instruments.^{15–17} This growth is also, in part, an overflow from the adoption of functional magnetic resonance imaging (fMRI)^{18,19} by these communities to study the functional organization of the human brain. fMRI has created a revolution in the study of the brain by enabling brain scientists to correlate neurophysical measures of the brain with behavioral measures. DOI complements fMRI by enabling functional brain imaging in subject populations and with study paradigms that are not easily studied, given the space confining and expense limitations of fMRI. In addition, DOI has the potential to provide more quantitative information about total hemoglobin concentration (proportional to cerebral blood volume) and hemoglobin oxygenation, as provided by optical absorption spectroscopy, than can be provided by fMRI.²⁰ This potential is further driving the technological development of DOI.

Diffuse optical methods were first used to measure

The authors are with the Athinoula A. Martinos Center for Biomedical Imaging, Massachusetts General Hospital, Harvard Medical School, Charlestown, Massachusetts 02129. D. A. Boas's e-mail address is dboas@nmr.mgh.harvard.edu.

Received 21 July 2004; revised manuscript received 16 November 2004; accepted 16 November 2004.

0003-6935/05/101957-12\$15.00/0

© 2005 Optical Society of America

brain activation in 1993.^{10,11} These first measurements used a maximum of five detector channels to measure the change in total hemoglobin concentration and oxygenation induced by a stimulus. The first diffuse optical images of brain activation were published in 1995.²¹ These first images were obtained by use of a backprojection method to interpolate the response between measurement channels^{21,22} such that the image resolution was approximately 3 cm, comparable with the distance between light sources and detectors. In addition, the quantitative accuracy of these images is limited by the partial volume effect^{23–25} in that the backprojection analysis does not account for the fact that the activation-induced change in the total hemoglobin concentration and oxygenation is occurring only in a small region of the tissue sampled by the diffuse light. The resolution and quantitative accuracy limitation can be overcome only by performing diffuse optical tomography (DOT), which uses a model of photon migration through the head to obtain an optimal image²⁶ of brain activation that is consistent with the set of measurements. To date, there are only a few published examples of DOT images of brain activation, for example, in rodents,^{27–30} in newborn human babies,¹⁴ and in adult humans.^{31,32}

Improvements in DOT image resolution and localization accuracy of brain activation will result from an increase in the number of measurements such that there are overlapping measurements of the same tissue regions.^{26,32} The quantitative accuracy of DOT is ultimately limited by the structural resolution. Inaccurate knowledge of the structural properties of the tissue will result in inaccurate models of photon migration through the tissue and thus in an inaccurate estimate of the brain-activation-induced change in the hemoglobin concentrations. In addition, the optical density and size of the adult human head precludes transmission measurements but permits reflectance measurements of diffuse light, which are predominantly sensitive to the superficial tissues. As a result, images are often biased toward the surface of the head, producing systematic depth localization errors and thus errors in the quantitative accuracy of the reconstructed hemoglobin concentrations. These limitations are perhaps best overcome by prior structural information.^{33–35}

In this paper we describe the results of photon migration imaging simulations on a three-dimensional (3D) anatomical head model provided by MRI. We implement concepts developed in the photon migration imaging community for improving image quality in general and specifically demonstrate their application to the problem of imaging adult human brain function. We demonstrate the improvement in localization accuracy and image resolution of cortical increases in optical absorption through the use of overlapping measurements. We also demonstrate that a spatial prior that constrains the optical image reconstruction to the cortex provides a significant improvement in the quantitative accuracy by forcing the image to be reconstructed at the appro-

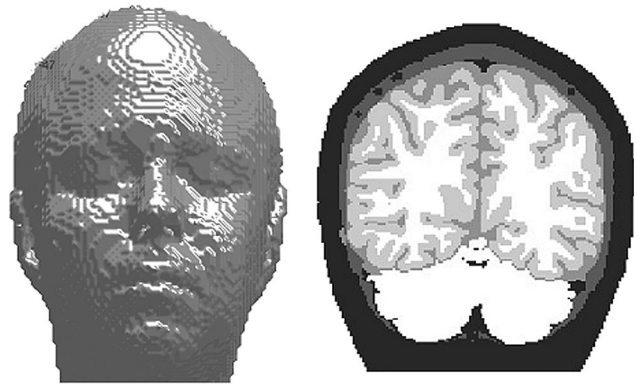


Fig. 1. Three-dimensional perspective of the head acquired by MRI is shown on the left. A coronal slice through the head is shown on the right, with the scalp, skull, cerebral spinal fluid, and gray and white matter indicated from dark to lighter shades of gray.

appropriate depth. While the results presented here are a straightforward implementation of previous research, we believe that these results are a necessary and important step toward specific experimental implementation of the concepts for functional imaging of the human brain.

2. Methods

We perform a Monte Carlo simulation of photon migration through a 3D head model provided by MRI. This simulation provides the predicted photon migration measurements (the forward solution) and the imaging operator for the inverse problem. These methods and the quantitative imaging metrics for assessing improvements in image quality are described in Subsections 2.A–2.E.

A. Tissue Segmentation of a Three-Dimensional Anatomical Magnetic Resonance Image

For our 3D model of the human head, we use a segmentation of an anatomical MRI based on an extension of the methods developed by Dale and Sereno,³⁶ Dale *et al.*,³⁷ and Fischl *et al.*³⁸ Dale and Fischl have implemented a multflip angle MRI pulse sequence that provides intrinsic T_1 and proton density maps with 3D isotropic 1-mm³ resolution. We have used these T_1 and proton density anatomical maps to produce the tissue segmentation shown in Fig. 1 by using a multispectral extension of the probabilistic segmentation approach described in Fischl *et al.*³⁸ The segmentation shows the scalp, skull, cerebral spinal fluid, and gray and white brain matter. For our simulation study, we assign a reduced scattering coefficient, μ_s' , and absorption coefficient, μ_a , to each tissue type, the values of which are indicated in Table 1. These values are the same ones that we have used previously²⁵ and are intermediate values of the wide variation of μ_a and μ_s' parameters that have been reported.^{39–41} We do not distinguish the optical properties of gray and white matter because our prelim-

Table 1. Optical Properties Used for Each Tissue Type in the Monte Carlo Simulation^a

Tissue	μ_s' (cm ⁻¹)	μ_a (cm ⁻¹)
Scalp	6.6	0.191
Skull	8.6	0.136
Cerebral spinal fluid	0.1	0.026
Gray and white matter	11.1	0.186

^aThe optical properties of the white matter are set equal to those of the gray matter in our simulations because the large variation in the properties of the white matter had a negligible effect on the measured fluence.

inary analysis has indicated that white matter properties do not significantly alter the results.

B. Photon Migration Forward Method

The appropriate treatment of the complex, nonplanar air-tissue and internal tissue boundaries is critical for accurate modeling of photon migration through the human head. Given the structural information provided by MRI, we can then solve the photon diffusion equation or radiative transport equation by using numerical approaches such as the finite difference, finite-element, and Monte Carlo methods. In this paper we use our implementation of a Monte Carlo solution of the radiative transport equation.⁴² This solution allows for spatially varying optical properties. This Monte Carlo code allows us to obtain results in a complex 3D head model with a signal-to-noise ratio greater than 100 at distances of up to 30 mm with a 1-mm² detector and with 10⁸ photons propagated within 5–10 h of computer time on a Pentium III 1000-MHz CPU (faster with today's newer desktop computers). Example results obtained with this Monte Carlo code can be found in Refs. 25, 42, and 43.

This computer code is used to calculate the continuous-wave detected photon fluence, $\Phi_o(\mathbf{r}_s, \mathbf{r}_d)$, and the photon absorption sensitivity profile, $G_{3pt}(\mathbf{r}_s, \mathbf{r}, \mathbf{r}_d)$, for each source-detector pair. As described in Refs. 26 and 42, this sensitivity profile, otherwise known as the three-point Greens' function, is calculated from the product of the fluence distribution $\Phi_{src}(\mathbf{r}_s, \mathbf{r})$ from the position of the light source, \mathbf{r}_s , into the 3D volume of the head, \mathbf{r} , and the fluence

distribution, $\Phi_{det}(\mathbf{r}, \mathbf{r}_d)$, from the position of the detector, \mathbf{r}_d , into the head. An example of these sensitivity profiles is given in Fig. 2.

The Rytov approximation indicates that the fluence in the presence of small spatial variations in the absorption coefficient is given by^{26,44}

$$\Phi(\mathbf{r}_s, \mathbf{r}_d) = \Phi_o(\mathbf{r}_s, \mathbf{r}_d)\exp[-\Phi_{pert}(\mathbf{r}_s, \mathbf{r}_d)], \quad (1)$$

where $\Phi_o(\mathbf{r}_s, \mathbf{r}_d)$ is the fluence calculated for the baseline properties of the head. The perturbation, $\Phi_{pert}(\mathbf{r}_s, \mathbf{r}_d)$, in the detected photon fluence caused by a localized change in the absorption coefficient $\delta\mu_a(\mathbf{r})$, is given by

$$\Phi_{pert}(\mathbf{r}_s, \mathbf{r}_d) = \frac{1}{\Phi_o(\mathbf{r}_s, \mathbf{r}_d)} \times \int \Phi_{src}(\mathbf{r}_s, \mathbf{r})\delta\mu_a(\mathbf{r})\Phi_{det}(\mathbf{r}, \mathbf{r}_d)d\mathbf{r}. \quad (2)$$

Thus, given the Monte Carlo estimates of $G_{3pt}(\mathbf{r}_s, \mathbf{r}, \mathbf{r}_d) = \Phi_{src}(\mathbf{r}_s, \mathbf{r})\Phi_{det}(\mathbf{r}, \mathbf{r}_d)$ and a spatial distribution of the localized changes in the absorption coefficient $\delta\mu_a(\mathbf{r})$ caused by brain activation, we can calculate the perturbation in the measurement $\Phi_{pert}(\mathbf{r}_s, \mathbf{r}_d)$. Brain activation produces only small absorption changes, and thus the Rytov model is expected to provide accurate results.

For the purposes of this paper, we consider a distribution of $\delta\mu_a(\mathbf{r})$ given by a 3D Gaussian with an isotropic full width at half-maximum of 1.0 cm, as illustrated below in Fig. 4, with a maximum of $\delta\mu_a = 0.01 \text{ cm}^{-1}$. The forward problem was calculated with 2 mm × 2 mm × 2 mm voxels throughout the medium for the forward and inverse problems.

C. Geometry of Sources and Detectors

We use a hexagonal arrangement of 15 sources and 32 detectors as shown in Fig. 3(a), which enables us to measure light from the 62 first and 52 second nearest-neighbor sources for a total of 114 measurements with a reasonable dynamic range requirement. The nearest-neighbor spacing between each source and detector is 2.5 cm, while the second nearest spac-

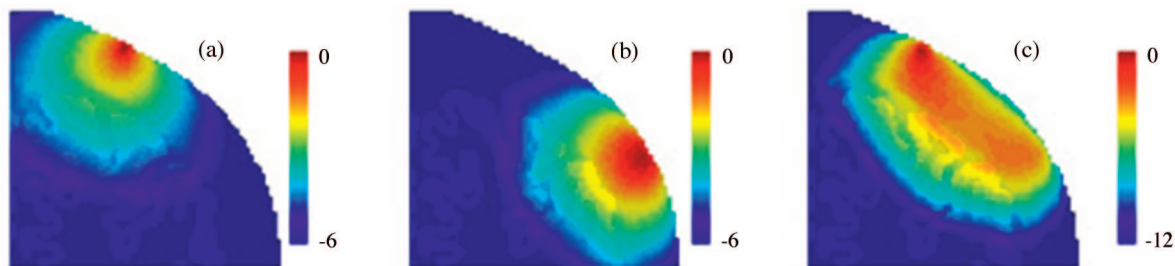


Fig. 2. (a) Source fluence distribution $\Phi_{src}(\mathbf{r}_s, \mathbf{r})$. (b) Detector fluence distribution $\Phi_{det}(\mathbf{r}, \mathbf{r}_d)$. (c) Measurement sensitivity profile for the given source and detector is given by the product of (a) and (b). The lighter curving structure inside the head indicates the gray matter. The color bar indicates the relative log10 decay of the sensitivity profile. Notice the logarithmic decay in sensitivity with depth. These results were calculated with a 1-mm³ resolution.

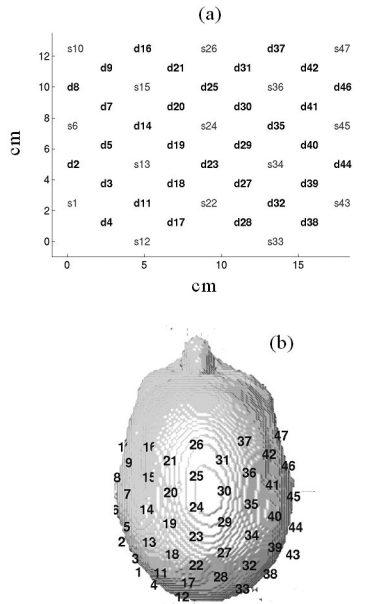


Fig. 3. Flattened arrangement of sources (s1, s2, etc.) and detectors (d2, d3, etc.) is shown in (a) such that the hexagonal arrangement is evident, as well as the overlap of the second nearest-neighbor measurements. The wrapping of the optode array over the top of the head is indicated in (b).

ing is 4.3 cm. As shown in Fig. 3(b), this probe is conformed to the curvature of the head over the left and right hemispheres of the parietal cortex. Conforming to the head causes a maximum deviation of these separations of less than 2 mm. From our measurements on adult human subjects with our continuous-wave imaging system,¹⁷ we estimate that the signal decrease from the shorter to the longer separation is roughly a factor of 10. As detailed in Ref. 32, we utilize a hexagonal arrangement because of a reduced dynamic range requirement for achieving overlapping measurements relative to a rectangular geometry.

D. Inverse Imaging Method

As described above for the photon migration forward method, for small changes in the spatial variation of the absorption coefficient, there is a linear relation between the perturbed photon fluence and the variation in the absorption coefficient. This relation can be written in matrix form as $\mathbf{y} = \mathbf{A}\mathbf{x}$, where the i th element of the vector \mathbf{y} corresponds to the perturbed photon fluence for the i th measurement, the j th element of the vector \mathbf{x} corresponds to the change in the absorption coefficient for the j th voxel of the head, and the matrix \mathbf{A} is derived from $G_{3\text{pt}}(\mathbf{r}_s, \mathbf{r}, \mathbf{r}_d)$ [Eq. (2)] and is the transformation from the image space to the measurement space. The forward method derives \mathbf{y} given \mathbf{x} . The inverse method is to estimate \mathbf{x} given \mathbf{y} .²⁶ This inversion is ill posed because the inversion process tends to amplify noise from \mathbf{y} in the image \mathbf{x} . Furthermore, the inversion is underdetermined because we have only 114 measurements in \mathbf{y} and more

than 10,000 unknowns in \mathbf{x} . As a result, the inverse problem must be regularized.

We estimate the optimal solution of \mathbf{x} by using²⁶

$$\hat{\mathbf{x}} = \mathbf{A}^T(\mathbf{A}\mathbf{A}^T + \lambda\sigma_y^2)^{-1}\mathbf{y} = \mathbf{B}\mathbf{y}, \quad (3)$$

where σ_y^2 is the measurement covariance matrix (assumed to be diagonal) and $\lambda = \alpha$ maximum [diagonal ($\mathbf{A}\mathbf{A}^T$)] is the scalar regularization parameter. The standard deviation of the measurements used to generate σ_y^2 was 0.1% for the nearest measurements and 1% for the second nearest measurements. This deviation is relative to the total measured fluence Φ from Eq. (1). All the images presented below are produced with noise-free data and with $\alpha = 0.01$ and the σ_y^2 given by assumed 0.1% and 1% standard deviations. The measurement noise is considered in the image contrast-to-noise ratio (CNR) metric used to evaluate image quality and the trade-off between image noise and resolution. The matrix \mathbf{B} is the pseudoinverse of \mathbf{A} .

The matrix \mathbf{A} can be written as $\mathbf{A} = [\mathbf{A}_{\text{noncortex}} \mathbf{A}_{\text{cortex}}]$, where $\mathbf{A}_{\text{noncortex}}$ has all voxels that are not within the cortex and $\mathbf{A}_{\text{cortex}}$ contains voxels only from the cortex. The inversion in Eq. (3) produces an image within all of the voxels of the head. We can impose a spatial prior to indicate that brain activation and the corresponding absorption change occurs only in the cortex by replacing \mathbf{A} in Eq. (3) with $\mathbf{A}_{\text{cortex}}$. We compare the image quality of these full head reconstructions with the cortically constrained reconstructions.

We also compare the images reconstructed within the head geometry against the images reconstructed assuming a semi-infinite medium, because this is a common approximation when the true geometry is not known.^{14,32} In this case we use the flat arrangement of sources and detectors depicted in Fig. 3(a) and calculate the matrix \mathbf{A} by using the analytic solution of the diffusion equation for a semi-infinite medium,²⁶ assuming $\mu_s' = 10 \text{ cm}^{-1}$ and $\mu_a = 0.1 \text{ cm}^{-1}$. In the semi-infinite medium we assume that the absorption changes are occurring in a plane beneath the plane of sources and detectors at a depth of 1.5 to 2.0 cm. The voxels are $0.1 \times 0.1 \text{ cm}$ in the lateral coordinates and 0.5 cm thick in depth. The plane of voxels only extends as far as the extent of sources and detectors.

To facilitate visualization of the 3D head reconstructions and comparison with the semi-infinite reconstructions, we perform a maximum intensity radial projection on each coronal slice of the absorption change image. An example of this is depicted in Fig. 4(a), which shows a single coronal slice of the absorption change with radial projections from the center of the head. The flattened projection image is depicted in Fig. 4(b), with the x coordinate depicting the distance along the scalp and the y coordinate depicting the different coronal slices.

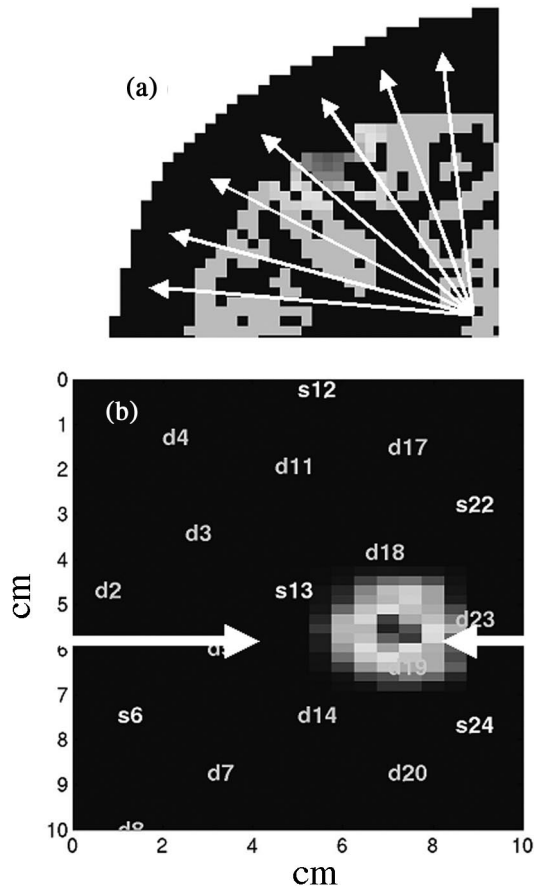


Fig. 4. (a) Coronal section is shown with the true activation-induced increase in cortical absorption. The maximum intensity radial projection is calculated slice by slice. The flattened projection is shown in (b), in which the coronal slice in (a) is indicated by the horizontal arrows. The lighter region inside the head indicates gray matter.

E. Metrics of Image Quality

The metrics of image quality that we utilize are image contrast, image CNR, image localization error, and image resolution full volume at half-maximum (FVHM). The image contrast and CNR are taken as the average of the image contrast and image noise over the FVHM. The image noise was determined by propagation of the measurement noise by $\sigma_x^2 = \mathbf{B}\sigma_y^2\mathbf{B}^T$, where σ_x^2 is the image covariance matrix and σ_y^2 is the measurement covariance. The localization error is determined from the contrast weighted distance of the voxels in the FVHM from the peak position and thus also serves as a measure of the resolution. That is,

$$\text{position error moment} = \sum_{i=1}^{N_{\text{vox}}} \frac{x_i r_i}{x_i} F(x_i > 0.5x_{\text{max}}),$$

where the sum is over all voxels; x_i is the contrast of the i th voxel; r_i is the distance of the i th voxel from the peak position of the true contrast; and the function F is 1 when $x_i > 0.5x_{\text{max}}$ and 0 otherwise, where

x_{max} is the maximum contrast in the reconstructed image \mathbf{x} .

3. Results

Example image reconstructions are shown in Figs. 5–7. The full head and cortically constrained images with only 62 nearest-neighbor measurements is shown in Fig. 5. The same with the 114 overlapping measurements is shown in Fig. 6, followed by the semi-infinite reconstructions in Fig. 7. The regularization parameter was set to $\alpha = 0.01$ for all reconstructions. The quantitative image metrics of contrast, CNR, and localization error versus the image regularization parameter α are shown in Fig. 8.

The cortically constrained image reconstruction ($\alpha = 0.01$), using overlapping measurements for a deeper brain activation, is shown in Fig. 9. The cortical constraint forces the contrast reconstruction into the cortex; however, the contrast is reconstructed in superficial rather than in deep cortex. A coronal slice of the image CNR is shown for comparison in Fig. 9(c). Notice that the CNR image is localized deeper toward the true activation.³⁷

The image metrics vary with the centroid position of the true absorption change. This variation within three different coronal slices is shown in Fig. 10 in which the value of the image metric is color coded and displayed in the cortical voxel that corresponds to the centroid position of the true absorption change. The position of the three slices relative to the sources and detectors is indicated in the top panel of Fig. 10.

4. Discussion

A. Improvement in Localization with Overlapping Measurements and Cortical Constraint

As shown in Figs. 5–7, the inclusion of overlapping measurements significantly improves the lateral localization accuracy. Without overlapping measurements, there is ambiguity as to whether the absorption change occurs close to the source, to the detector, or in between. Overlapping measurements resolve this ambiguity with a two-fold improvement in localization accuracy, as shown in the image metric in Fig. 8. This improvement has also been quantified in Refs. 32 and 45.

The example shown in Figs. 5 and 7, with the absorption change occurring in the void region between three detectors of the hexagonal probe that is not strongly sampled with nearest-neighbor sources, is a worst-case scenario. An absorption change occurring in this region will be pulled in three separate directions toward the three different sources in the image reconstructed with only the nearest-neighbor measurements. There are other probe geometries that do not create such a large localization ambiguity when overlapping measurements are not used. In particular, the rectangular style geometry that is currently used almost universally for DOI of brain function.^{8,9,21,30,45} Nonetheless, even with rectangular geometries, there is a strong improvement in the localization accuracy with the use of overlapping

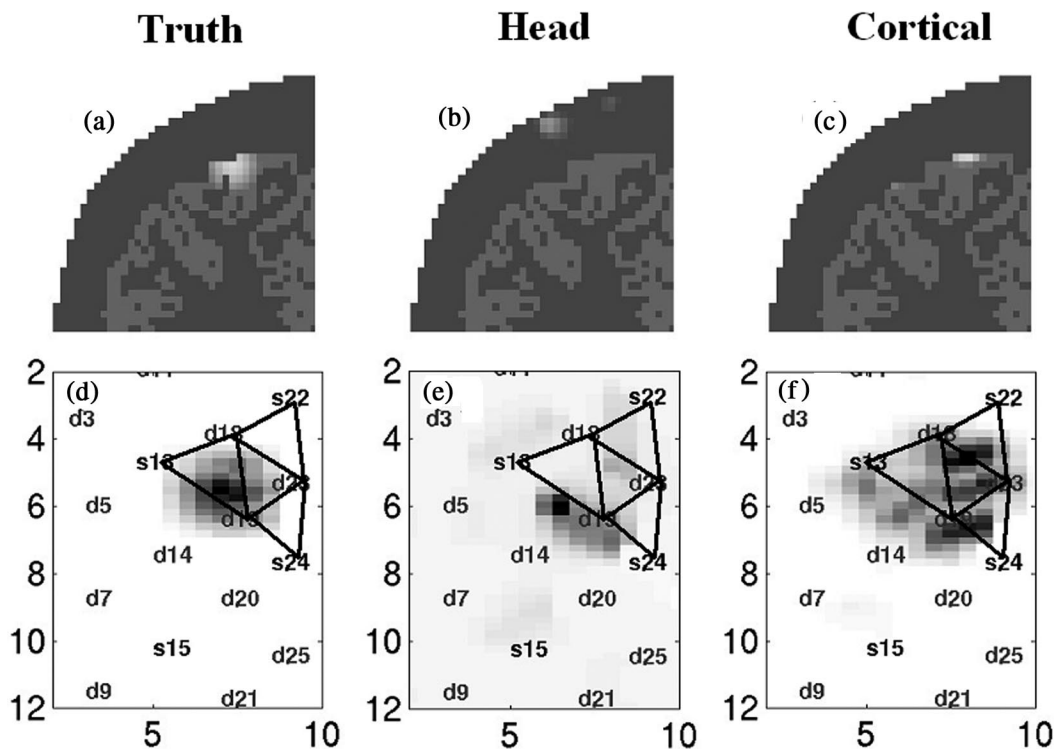


Fig. 5. Images reconstructed with the first nearest-neighbor measurements. The true cortical absorption change is shown in (a) coronal and (d) radial projection views. The reconstructed full head images in (b) and (e) show poor lateral and depth localization of the absorption change. The cortically constrained reconstruction shown in (c) and (f) still has poor localization as a result of spatial ambiguity arising from utility of only the nearest-neighbor measurements. The lighter gray region in (a), (b), and (c) indicates the gray matter. The length scale in (d), (e), and (f) is in centimeters. The scales in each figure are normalized. The quantitative comparison of contrast magnitude is shown in Fig. 8.

measurements, as has been quantified in Refs. 32 and 45.

Depth localization is quite difficult in DOI of brain function, given that only reflectance measurements are achievable in adults. Depth resolution can be slightly improved when source–detector pairs are utilized at different separations because measurements with small separations sample only superficial tissues, while measurements with larger separations sample deeper tissues.^{40,46} Better improvement in depth resolution can be achieved with time-resolved measurements of photon transit time because deeper tissues are sampled with longer photon transit times.^{24,46,47} However, this paper focuses only on continuous-wave measurements, which currently constitute the majority of published brain function measurements (there are only a couple of published examples of depth-resolved brain imaging with time-resolved measurements^{24,47–49}). As shown in Fig. 5, the nearest-neighbor image reconstructs the absorption change at the surface. This is a common problem with minimum-norm-type image reconstructions, which bias the reconstructed image toward regions of maximum sensitivity. Thus images are biased toward the surface because maximum sensitivity is found near the surface, near sources and detectors. The addition of overlapping measurements pushes the reconstructed absorption

change deeper into the head (see Fig. 6) by providing additional complimentary information to the image reconstruction such that image consistency with the data results in better depth localization. However, the reconstructed absorption change is still superficial to the cortex.

Since we know that the absorption change arising from cortical activation should not happen superficial to the cortex, a depth prior can be introduced into the image reconstruction. This can be accomplished statistically in the form of depth-dependent spatial regularization^{50,51} or as a hard structural constraint, as we do here and as discussed previously in the context of breast imaging^{33,52} and brain imaging.³⁴ This is easily achieved when we are assuming a simple semi-infinite medium model of the head by reconstructing the absorption change only in a single slice at the approximate average depth of the cortex. However, as we see from Fig. 7, while the peak absorption change is approximately located in the correct position with overlapping measurements, there are still strong image artifacts spreading toward the other nearby sources, presumably as a result of model mismatch between the human head and the assumed semi-infinite medium. Anecdotally, we often observe such image artifacts in our optical brain function images when assuming a semi-infinite medium, thus rendering it difficult to find a good spatial correlation with

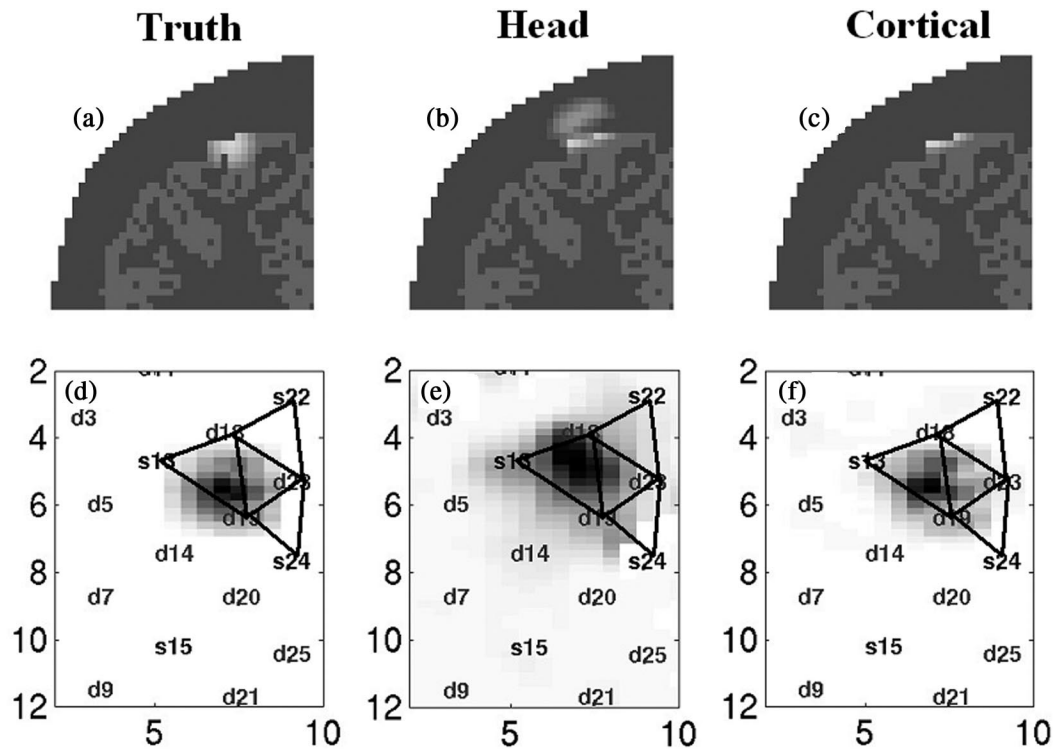


Fig. 6. Images reconstructed with overlapping (first and second nearest-neighbor) measurements show much better localization relative to images reconstructed with only the first nearest measurements (Fig. 5). In particular, the projection of the cortically constrained reconstruction (f) is strikingly similar to that of the true projection. The discontinuity observed in (b) reflects the structure of the cerebral spinal fluid in which the measurement sensitivity is reduced relative to the surrounding tissue. The lighter gray region in (a), (b), and (c) indicates gray matter. The length scale in (d), (e), and (f) is in centimeters.

fMRI.^{53,54} The proper cortical structural constraint produces an image that, at least in the maximum intensity radial projection, looks remarkably similar to the true image in terms of position and spatial extent [see Fig. 6(f)]. However, the coronal cross section [Fig. 6(c)] reveals that the reconstructed image is pulled toward the surface of the cortex. This is amplified further in the example of a deeper cortical activation [see Fig. 9(b)].

Improved depth accuracy is found in the CNR image [see Fig. 9(c)]. However the contrast within the region of interest defined by the FVHM of the CN image is significantly reduced relative to the true contrast as the significant portion of the reconstructed contrast is pulled to the surface of the cortex. One could use the CNR image as a statistical spatial prior within the cortical constraint, similar to what was done in Ref. 55, to bias the image in order to reconstruct deeper within the cortex. One could also use an fMRI image of the blood-oxygen-level-dependent signal or blood flow response to brain activation as a statistical spatial prior to the optical image reconstruction. Both approaches are left for future work. An additional approach uses time-domain measurements with ~ 100 -ps temporal resolution of pulsed laser light propagation through tissue to provide depth resolution. This approach has been described by Steinbrink *et al.*²⁴ and Kohl *et*

*al.*⁴⁷ and shows promise for providing depth localization accuracy without prior spatial information.

B. Variation of Image Metrics with Regularization

As shown in Fig. 8, with regularization of $\alpha < 0.1$ the cortical constraint image reconstruction of overlapping measurements underestimates the correct absorption contrast by only 10%, compared with 40% for the nearest-neighbor measurements only and 90% without the cortical constraint. The large error observed without the cortical constraint clearly occurs because the contrast is reconstructed closer to the surface where there is greater sensitivity to an absorption change. Likewise, the cortical constraint of only nearest-neighbor measurements reconstructs the contrast closer to the scalp surface where the sensitivity is greater and thus produces a smaller contrast image. The contrast reconstructed with the semi-infinite medium model is not shown as model error in the structure of the optical properties of the medium; in particular, the depth of the cortex produces an image error of more than an order of magnitude. This severe sensitivity to depth has been discussed in Ref. 56.

Of interest is that, while the best contrast is reconstructed for the cortical constraint of overlapping measurements with $\alpha < 0.1$, this image has the smallest CNR. This is a result of the image being

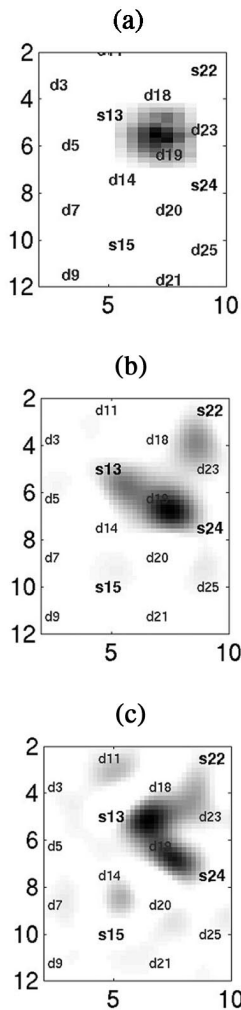


Fig. 7. (a) True head geometry, (b) first nearest-neighbor measurements, (c) first and second nearest-neighbor measurements. Semi-infinite reconstructions show poor spatial localization of the activation, even with the overlapping measurements, owing to model mismatch between the true head geometry and the homogeneous semi-infinite medium. The length scale is in centimeters.

reconstructed in a region of less sensitivity relative to the three other image conditions. Increasing the regularization increases the CNR but reduces the reconstructed contrast, usually at the expense of image resolution but also by pulling the reconstructed contrast to regions of higher measurement sensitivity. Notice that as the regularization increases, the overlapping measurement image metric converges to that of the nearest-neighbor measurement. This happens because increasing regularization first acts on the more distant measurements, which have a smaller signal-to-noise ratio. A regularization parameter of $0.01 < \alpha < 0.1$ provides the best trade-off between an accurate contrast and a decent CNR.

For $\alpha < 0.1$ the positional error moment is approximately 5 mm for the cortically constrained reconstruction of overlapping measurements. Increasing the regularization parameter diminishes this accuracy because the reconstructed contrast is pulled toward regions of higher measurement sensitivity.

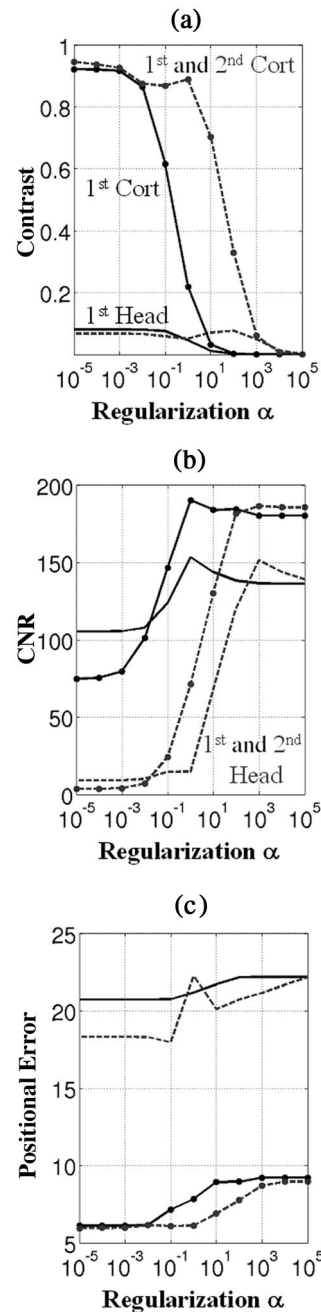


Fig. 8. Variation in image contrast and CNR with regularization is shown in (a) and (b), respectively. The contrast is shown in units relative to the peak absorption change of 0.01 cm^{-1} . The CNR is given in standard deviation units such that a CNR of 100 means that the reconstructed contrast is 100 times greater than the standard deviation in the image contrast. The variation in localization error and FWHM with regularization is shown as the moment of the positional error in (c). The positional error is given in units of millimeters. Nearest-neighbor results are shown by the solid curves. Overlapping measurements are shown by the dashed curves. The cortically constrained results are distinguished from the full head results by the curves with filled circles.

C. Spatial Variation in Image Metrics

The spatial variation in the image CNR shown in Fig. 10 shows the expected result that CNR is greater

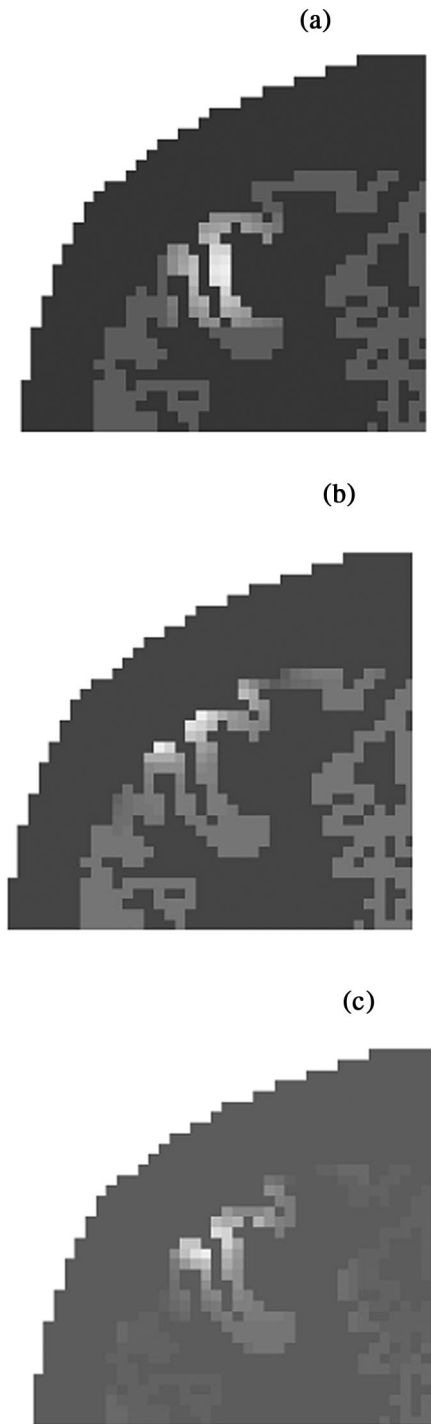


Fig. 9. Cortically constrained reconstructed contrast (b) of a deeper (true) activation shown in (a) is pulled toward the outer surface of the cortex where measurement sensitivity is greatest. The image CNR shown in (c) reveals a better depth localization than the image contrast. The lighter gray region in (a), (b), and (c) indicates gray matter.

where the measurement sensitivity is greater. This occurs near the sources for the hexagonal geometry because each source is measured by 12 detectors. Al-

ternatively, each detector sees four different sources. Thus the region near a source is sampled 3 times more than a region near a detector, and thus we find greater image CNRs near the sources. The image CNR drops exponentially with depth in concert with the exponential drop in measurement sensitivity with depth.

The positional error increases with depth since deeper absorption changes are pulled toward the surface of the brain. It is interesting that the positional error is fairly uniform for a given depth into the brain, indicating that the lateral localization accuracy varies little with lateral position relative to the sources and detectors when overlapping measurements are used. This is in significant contrast to the large spatial variation in lateral positional error obtained when imaging with only nearest-neighbor measurements.³²

D. Uncertainty in the Background Optical Properties

Uncertainty in the estimate of the static background optical properties of each tissue will cause a systematic error in the predicted optical measurement sensitivity to brain activation in the cortex. As a result, the reconstructed image contrast and position have a systematic error. We explored the magnitude of this effect in a simplified geometry in Cheng and Boas.⁵⁶ In this paper we found that a 20% uncertainty in the static optical properties of the medium caused an approximately equal uncertainty in the estimated change in the absorption coefficient. We repeated this estimate for the more complex head geometry shown in Fig. 1, varying the absorption and scattering properties of each tissue type individually, and similarly found that the systematic error in the image contrast was approximately equal to the systematic error in the optical properties of each tissue type. We did not compile those results here because they were quite similar to the simplified geometry discussed in Ref. 56.

We are working on using time-domain measurements guided by structural MRI to accurately characterize the static optical properties of each tissue type. Our simulation study has shown that an estimate of the static optical properties with an uncertainty less than 20% is reasonably achieved with current instrument specifications.³⁵ This estimate, however, does not account for systematic error in the segmentation of the structural MRI into distinct tissue types. This will have to be addressed in the future.

5. Summary

We have combined concepts established in the literature for improving image quality and have quantified through simulations the improvement afforded for the specific application of imaging adult human brain activation. We have shown in a 3D realistic head model that overlapping continuous-wave measurements provide significant improvements in lateral localization and some improvement in depth localization without a cortical constraint. However, the depth of the cortical absorption increase is still

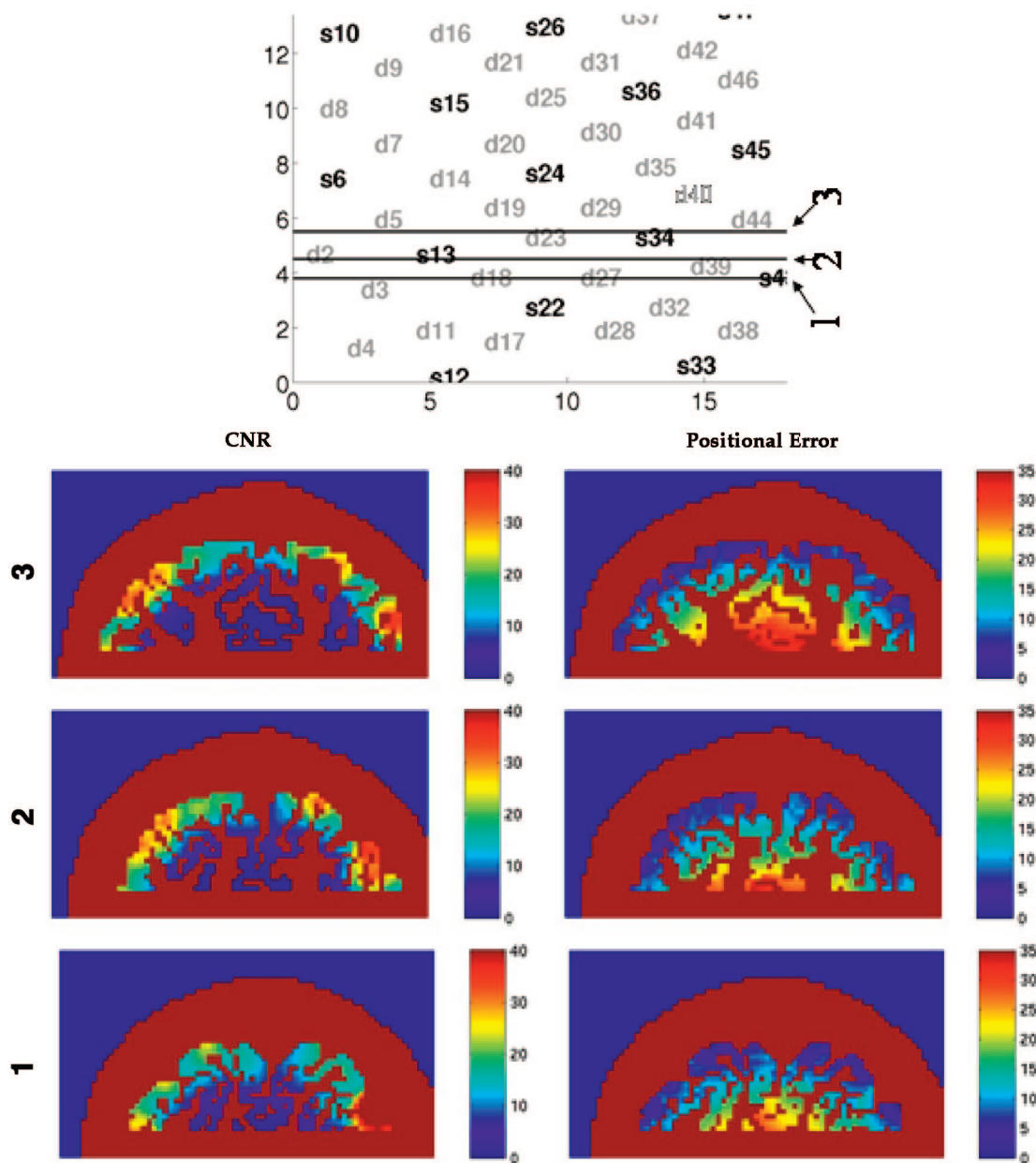


Fig. 10. Image metrics vary with position in the brain. This variation is shown for the image CNR (standard deviation units) and the positional error (in millimeters) in three coronal slices with different positions relative to the sources and detectors. The image CNR is greatest in regions near the sources, whereas the positional error increases rapidly with depth but shows little variation at a given depth.

significantly underestimated. This depth underestimation then results in a significant underestimation of the absorption contrast. With continuous-wave measurements, a spatial cortical constraint is required to localize cortical absorption changes in the cortex. We have shown that with a cortical constraint it is possible to reconstruct the absorption contrast with quantitative accuracy when the true absorption contrast is near the superficial cortex close to the skull. However, when the true contrast is deeper, despite the cortical constraint, the absorption contrast is reconstructed more superficially within the cortex, leading to an underestimation of the absorption amplitude. While the CNR image does slightly

improve the depth localization accuracy, it is likely that a functional MRI spatial constraint within the cortex is required to achieve an accurate estimate of the absorption contrast. Time-domain measurements have been shown to provide depth-resolution accuracy and may provide an alternative approach to achieving quantitatively accurate estimates of cortical absorption changes.

D. A. Boas thanks Simon Arridge for many useful conversations related to the general ideas presented in this paper. This study was supported by National Institutes of Health grants P41-RR14075, R01-EB002482, and R01-EB00790.

References

1. A. A. Baird, J. Kagan, T. Gaudette, K. A. Walz, N. Hershlag, and D. A. Boas, "Frontal lobe activation during object permanence: data from near-infrared spectroscopy," *Neuroimage*, **16**, 1120–1125 (2002).
2. H. Kato, M. Izumiyama, H. Koizumi, A. Takahashi, and Y. Itoyama, "Near-infrared spectroscopic topography as a tool to monitor motor reorganization after hemiparetic stroke: a comparison with functional MRI," *Stroke*, **33**, 2032–2036 (2002).
3. I. Miyai, H. Yagura, I. Oda, I. Konishi, H. Eda, T. Suzuki, and K. Kubota, "Premotor cortex is involved in restoration of gait in stroke," *Ann. Neurol.*, **52**, 188–194 (2002).
4. G. Gratton, M. Fabiani, T. Elbert, and B. Rockstroh, "Seeing right through you: applications of optical imaging to the study of the human brain," *Psychophysiology*, **40**, 487–491 (2003).
5. A. F. Cannestra, I. Wartenburger, H. Obrig, A. Villringer, and A. W. Toga, "Functional assessment of Broca's area using near infrared spectroscopy in humans," *NeuroReport*, **14**, 1961–1965 (2003).
6. M. Moosmann, P. Ritter, I. Krastel, A. Brink, S. Thees, F. Blankenburg, B. Taskin, H. Obrig, and A. Villringer, "Correlates of alpha rhythm in functional magnetic resonance imaging and near infrared spectroscopy," *Neuroimage*, **20**, 145–158 (2003).
7. M. Wolf, U. Wolf, J. H. Choi, V. Toronov, L. A. Paunescu, A. Michalos, and E. Gratton, "Fast cerebral functional signal in the 100-ms range detected in the visual cortex by frequency-domain near-infrared spectrophotometry," *Psychophysiology*, **40**, 521–528 (2003).
8. G. Taga, K. Asakawa, A. Maki, Y. Konishi, and H. Koizumi, "Brain imaging in awake infants by near-infrared optical topography," *Proc. Natl. Acad. Sci. USA*, **100**, 10722–10727 (2003).
9. M. Pena, A. Maki, D. Kovacic, G. Dehaene-Lambertz, H. Koizumi, F. Bouquet, and J. Mehler, "Sounds and silence: an optical topography study of language recognition at birth," *Proc. Natl. Acad. Sci. USA*, **100**, 11702–11705 (2003).
10. A. Villringer, J. Planck, C. Hock, L. Schleinkofer, and U. Dirnagl, "Near infrared spectroscopy (NIRS): a new tool to study hemodynamic changes during activation of brain function in human adults," *Neurosci. Lett.*, **154**, 101–104 (1993).
11. Y. Hoshi and M. Tamura, "Detection of dynamic changes in cerebral oxygenation coupled to neuronal function during mental work in man," *Neurosci. Lett.*, **150**, 5–8 (1993).
12. J. H. Meek, M. Firbank, C. E. Elwell, J. Atkinson, O. Braddick, and J. S. Wyatt, "Regional hemodynamic responses to visual stimulation in awake infants," *Pediatr. Res.*, **43**, 840–843 (1998).
13. K. Sakatani, S. Chen, W. Lichty, H. Zuo, and Y. P. Wang, "Cerebral blood oxygenation changes induced by auditory stimulation in newborn infants measured by near infrared spectroscopy," *Early Hum. Dev.*, **55**, 229–236 (1999).
14. S. R. Hintz, D. A. Benaron, A. M. Siegel, A. Zourabian, D. K. Stevenson, and D. A. Boas, "Bedside functional imaging of the premature infant brain during passive motor activation," *J. Perinat. Med.*, **29**, 335–343 (2001).
15. G. Gratton, A. J. Sarno, E. Maclin, P. M. Corballis, and M. Fabiani, "Toward non-invasive 3-D imaging of the time course of cortical activity: investigation of the depth of the event-related optical signal (EROS)," *Neuroimage*, **11**, 491–504 (2000).
16. H. Koizumi, T. Yamamoto, A. Maki, Y. Yamashita, H. Sato, H. Kawaguchi, and N. Ichikawa, "Optical topography: practical problems and new applications," *Appl. Opt.*, **42**, 3054–3062 (2003).
17. M. A. Franceschini, S. Fantini, J. H. Thompson, J. P. Culver, and D. A. Boas, "Hemodynamic evoked response of the sensorimotor cortex measured noninvasively with near infrared optical imaging," *Psychophysiology*, **40**, 548–560 (2003).
18. K. K. Kwong, J. W. Belliveau, D. A. Chesler, I. E. Goldberg, R. M. Weisskoff, B. P. Poncelet, D. N. Kennedy, B. E. Hoppel, M. S. Cohen, R. Turner, H.-M. Cheng, T. J. Brady, and B. R. Rosen, "Dynamic magnetic resonance imaging of human brain activity during primary sensory stimulation," *Proc. Natl. Acad. Sci. USA*, **89**, 5675–5679 (1992).
19. S. Ogawa, D. Tank, R. Menon, J. Ellermann, S.-G. Kim, H. Merkle, and K. Ugurbil, "Intrinsic signal changes accompanying sensory stimulation: functional brain mapping with magnetic resonance imaging," *Proc. Natl. Acad. Sci. USA*, **89**, 5951–5955 (1992).
20. A. Villringer and B. Chance, "Non-invasive optical spectroscopy and imaging of human brain function," *Trends Neurosci.*, **20**, 435–442 (1997).
21. A. Maki, Y. Yamashita, Y. Ito, E. Watanabe, Y. Mayanagi, and H. Koizumi, "Spatial and temporal analysis of human motor activity using noninvasive NIR topography," *Med. Phys.*, **22**, 1997–2005 (1995).
22. M. A. Franceschini, V. Toronov, M. Filiaci, E. Gratton, and S. Fantini, "On-line optical imaging of the human brain with 160-ms temporal resolution," *Opt. Express*, **6**, 49–57 (2000), <http://www.opticsexpress.org>.
23. M. Hiraoka, M. Firbank, M. Essenpreis, M. Cope, S. R. Arridge, P. van der Zee, and D. T. Delpy, "A Monte Carlo investigation of optical pathlength in inhomogeneous tissue and its application to near-infrared spectroscopy," *Phys. Med. Biol.*, **38**, 1859–1876 (1993).
24. J. Steinbrink, H. Wabnitz, H. Obrig, A. Villringer, and H. Rinneberg, "Determining changes in NIR absorption using a layered model of the human head," *Phys. Med. Biol.*, **46**, 879–896 (2001).
25. G. Strangman, M. A. Franceschini, and D. A. Boas, "Factors affecting the accuracy of near-infrared spectroscopy concentration calculations for focal changes in oxygenation parameters," *Neuroimage*, **18**, 865–879 (2003).
26. S. R. Arridge, "Optical tomography in medical imaging," *Inverse Probl.*, **15**, R41–R93 (1999).
27. A. M. Siegel, J. J. A. Marota, and D. A. Boas, "Design and evaluation of a continuous-wave diffuse optical tomography system," *Opt. Express*, **4**, 287–298 (1999), <http://www.opticsexpress.org>.
28. A. M. Siegel, J. P. Culver, J. B. Mandeville, and D. A. Boas, "Temporal comparison of functional brain imaging with diffuse optical tomography and fMRI during rat forepaw stimulation," *Phys. Med. Biol.*, **48**, 1391–1403 (2003).
29. J. P. Culver, T. Durduran, D. Furuya, C. Cheung, J. H. Greenberg, and A. G. Yodh, "Diffuse optical tomography of cerebral blood flow, oxygenation, and metabolism in rat during focal ischemia," *J. Cereb. Blood Flow Metab.*, **23**, 911–924 (2003).
30. J. P. Culver, A. M. Siegel, J. J. Stott, and D. A. Boas, "Volumetric diffuse optical tomography of brain activity," *Opt. Lett.*, **28**, 2061–2063 (2003).
31. A. Bluestone, G. Abdoulaev, C. Schmitz, R. Barbour, and A. Hielscher, "Three-dimensional optical tomography of hemodynamics in the human head," *Opt. Express*, **9**, 272–286 (2001), <http://www.opticsexpress.org>.
32. D. A. Boas, K. Chen, D. Grebert, and M. A. Franceschini, "Improving diffuse optical imaging spatial resolution of cerebral hemodynamic response to brain activation in humans," *Opt. Lett.*, **29**, 1506–1508 (2004).
33. R. L. Barbour, H. L. Graber, J. Chang, S. S. Barbour, P. C. Koo, and R. Aronson, "MRI-guided optical tomography: prospects and computation for a new imaging method," *IEEE Comput. Sci. Eng.*, **2**, 63–77 (1995).
34. B. W. Pogue and K. D. Paulsen, "High-resolution near-infrared tomographic imaging simulations of the rat cranium by use of

- a priori* magnetic resonance imaging structural information,” *Opt. Lett.* **23**, 1716–1718 (1998).
35. A. H. Barnett, J. P. Culver, A. G. Sorensen, A. Dale, and D. A. Boas, “Robust inference of baseline optical properties of the human head with three-dimensional segmentation from magnetic resonance imaging,” *Appl. Opt.* **42**, 3095–3108 (2003).
 36. A. M. Dale and M. I. Sereno, “Improved localization of cortical activity by combining EEG and MEG with MRI cortical surface reconstructions: a linear approach,” *J. Cogn. Neurosci.* **5**, 162–176 (1993).
 37. A. M. Dale, A. K. Liu, B. R. Fischl, R. L. Buckner, J. W. Belliveau, J. D. Lewine, and E. Halgren, “Dynamic statistical parametric mapping: combining fMRI and MEG for high-resolution imaging of cortical activity,” *Neuron* **26**, 55–67 (2000).
 38. B. Fischl, D. H. Salat, E. Busa, M. Albert, M. Dieterich, C. Haselgrove, A. van der Kouwe, R. Killiany, D. Kennedy, S. Klaveness, A. Montillo, N. Makris, B. Rosen, and A. M. Dale, “Whole brain segmentation: automated labeling of neuroanatomical structures in the human brain,” *Neuron* **33**, 341–355 (2002).
 39. A. Torricelli, A. Pifferi, P. Taroni, E. Giambattistelli, and R. Cubeddu, “*In vivo* optical characterization of human tissues from 610 to 1010 nm by time-resolved reflectance spectroscopy,” *Phys. Med. Biol.* **46**, 2227–2237 (2001).
 40. E. Okada, M. Firbank, M. Schweiger, S. R. Arridge, M. Cope, and D. T. Delpy, “Theoretical and experimental investigation of near-infrared light propagation in a model of the adult head,” *Appl. Opt.* **36**, 21–31 (1997).
 41. F. Bevilacqua, D. Pignatelli, P. Marquet, J. D. Gross, B. J. Tromberg, and C. Depeursinge, “*In vivo* local determination of tissue optical properties: applications to human brain,” *Appl. Opt.* **38**, 4939–4950 (1999).
 42. D. A. Boas, J. Culver, J. Stott, and A. K. Dunn, “Three dimensional Monte Carlo code for photon migration through complex heterogeneous media including the adult head,” *Opt. Express* **10**, 159–170 (2002), <http://www.opticsexpress.org>.
 43. M. A. Franceschini and D. A. Boas, “Noninvasive measurement of neuronal activity with near-infrared optical imaging,” *Neuroimage*. **21**, 372–386 (2004).
 44. A. C. Kak and M. Slaney, *Principles of Computerized Tomographic Imaging* (Institute of Electrical and Electronics Engineers, New York, 1988).
 45. T. Yamamoto, A. Maki, T. Kadoya, Y. Tanikawa, Y. Yamada, E. Okada, and H. Koizumi, “Arranging optical fibres for the spatial resolution improvement of topographical images,” *Phys. Med. Biol.* **47**, 3429–3440 (2002).
 46. A. Kienle, M. S. Patterson, N. Dognitz, R. Bays, G. Wagnieres, and H. van den Bergh, “Noninvasive determination of the optical properties of two-layered turbid media,” *Appl. Opt.* **37**, 779–791 (1998).
 47. M. Kohl-Bareis, H. Obrig, J. Steinbrink, J. Malak, K. Uludag, and A. Villringer, “Noninvasive monitoring of cerebral blood flow by a dye bolus method: separation of brain from skin and skull signals,” *J. Biomed. Opt.* **7**, 464–470 (2002).
 48. S. R. Arridge, J. C. Hebden, M. Schweiger, F. E. W. Schmidt, M. E. Fry, E. M. C. Hillman, H. Dehghani, and D. T. Delpy, “A method for 3D time-resolved optical tomography,” *Int. J. Imaging Syst. Technol.* **11**, 2–11 (2000).
 49. J. C. Hebden, A. Gibson, R. M. Yusof, N. Everdell, E. M. Hillman, D. T. Delpy, S. R. Arridge, T. Austin, J. H. Meek, and J. S. Wyatt, “Three-dimensional optical tomography of the premature infant brain,” *Phys. Med. Biol.* **47**, 4155–4166 (2002).
 50. S. R. Arridge and M. Schweiger, “Inverse methods for optical tomography” in *Information Processing in Medical Imaging '93*, H. H. Barrett and A. F. Gmitro, eds. (Springer-Verlag, Berlin, 1993).
 51. B. W. Pogue, T. O. McBride, J. Prewitt, U. L. Osterberg, and K. D. Paulsen, “Spatially variant regularization improves diffuse optical tomography,” *Appl. Opt.* **38**, 2950–2961 (1999).
 52. V. Ntziachristos, A. G. Yodanis, M. Schnall, and B. Chance, “MRI-guided diffuse optical spectroscopy of malignant and benign breast lesions,” *Neoplasia* **4**, 347–354 (2002).
 53. V. Toronov, A. Webb, J. H. Choi, M. Wolf, L. Safonova, U. Wolf, and E. Gratton, “Study of local cerebral hemodynamics by frequency-domain near-infrared spectroscopy and correlation with simultaneously acquired functional magnetic resonance imaging,” *Opt. Express* **9**, 417–427 (2001), <http://www.opticsexpress.org>.
 54. G. Strangman, J. P. Culver, J. H. Thompson, and D. A. Boas, “A quantitative comparison of simultaneous BOLD fMRI and NIRS recordings during functional brain activation,” *Neuroimage*. **17**, 719–731 (2002).
 55. A. Li, E. L. Miller, M. E. Kilmer, T. J. Brukilacchio, T. Chaves, J. Stott, Q. Zhang, T. Wu, M. Chorlton, R. H. Moore, D. B. Kopans, and D. A. Boas, “Tomographic optical breast imaging guided by three-dimensional mammography,” *Appl. Opt.* **42**, 5181–5190 (2003).
 56. X. Cheng and D. A. Boas, “Systematic diffuse optical image errors resulting from uncertainty in the background optical properties,” *Opt. Express* **4**, 299–307 (1999), <http://www.opticsexpress.org>.